


Cite this: *Catal. Sci. Technol.*, 2019,  
9, 803

# Oxygen vacancy-rich $\text{MoO}_{3-x}$ nanobelts for photocatalytic $\text{N}_2$ reduction to $\text{NH}_3$ in pure water†

Yehuan Li,<sup>a</sup> Xin Chen,<sup>a</sup> Mingjian Zhang,<sup>a</sup> Yuanmin Zhu,<sup>b</sup> Wenju Ren,<sup>a</sup> Zongwei Mei,<sup>\*a</sup>  
Meng Gu <sup>\*b</sup> and Feng Pan <sup>\*a</sup>

Photocatalytic nitrogen fixation is a promising sustainable and green strategy for  $\text{NH}_3$  synthesis. The development of an efficient photocatalyst is the key to make this approach applicable. In this work,  $\text{MoO}_{3-x}$  nanobelts are synthesized by a hydrothermal method, and they are firstly utilized as photocatalysts for  $\text{N}_2$  fixation without using sacrificial reagents and precious-metal co-catalysts at room temperature and atmospheric pressure. It is found that oxygen vacancies ( $\text{O}_{\text{VS}}$ ) are located on the (001) and (100) planes by STEM analysis. The surface  $\text{O}_{\text{VS}}$  can chemisorb the  $\text{N}_2$  molecules by a side-on model on (001) while an end-on model on the (100) plane and elongate their bond length, playing a critical role in the photocatalytic  $\text{N}_2$  fixation activity. This result provides a new insight into developing efficient photocatalysts with original oxygen vacancies.

Received 17th November 2018,  
Accepted 10th January 2019

DOI: 10.1039/c8cy02357c

rsc.li/catalysis

## Introduction

Nitrogen fixation such as  $\text{N}_2$  reduction to  $\text{NH}_3$  is an important artificial synthesis in the chemical industry.<sup>1</sup> However, the industrial synthetic strategies consume a large amount of the world's annual energy supply and release large quantities of  $\text{CO}_2$  aggravating global climate change.<sup>2</sup> After the first report by Schrauzer and Guth in 1977, the photocatalytic  $\text{N}_2$  reduction to  $\text{NH}_3$  has attracted extensive research interest and shown high potential as a sustainable and green solution compared with the industrial Haber–Bosch process.<sup>3</sup> However, the photocatalytic activity of  $\text{N}_2$  fixation is still not satisfactory due to the high reaction activation energy barriers and hard cleavage of the strong  $\text{N}\equiv\text{N}$  triple bond energy ( $941 \text{ kJ mol}^{-1}$ ) of  $\text{N}_2$  molecules.<sup>4</sup>

It is well-known that crystal defect engineering has shown positive effects on many kinds of photocatalytic reactions,<sup>5</sup> and oxygen vacancies ( $\text{O}_{\text{VS}}$ ) are one of the most widely used defects.<sup>6–8</sup> There are three main kinds of ways to generate  $\text{O}_{\text{VS}}$  for photocatalytic experiments. Generally,  $\text{O}_{\text{VS}}$  could be formed *via* hydrothermal or solvothermal treatment naturally. For example, Tian *et al.* reported oxygen vacancy-rich

$\text{BiPO}_4$  through a one-pot solvothermal treatment for MB degradation.<sup>9</sup> Additionally, thermal treatment in hydrogen or inert gases is also a usual method to modulate the surface  $\text{O}_{\text{VS}}$  of samples.<sup>10</sup> Chen and co-workers enhanced the photocatalytic performances of  $\text{TiO}_2$  nanocrystals for methylene blue degradation and water splitting by generating  $\text{O}_{\text{VS}}$  in a hydrogen atmosphere and proved that the generation of  $\text{O}_{\text{VS}}$  was positive in enhancing light absorption.<sup>11</sup> Moreover, Ding *et al.* demonstrated that a triple atom defect cluster ( $\text{Br,Bi,O}$ ) on  $\text{BiOBr}$  could promote the generation of singlet oxygen through an energy transfer process. It resulted in an excellent conversion rate and selectivity in the sulfoxidation reaction.<sup>12</sup>

It has been demonstrated that the assistant electron-donating center can firstly capture the  $\text{N}_2$  molecules and weaken the  $\text{N}\equiv\text{N}$  triple bond, and then the photogenerated electrons accumulate in the capture sites to reduce the  $\text{N}_2$  into  $\text{NH}_3$ .<sup>13,14</sup> Many research results have revealed that oxygen vacancies can also act as electron trap sites and activate the inert  $\text{N}_2$ . For example, Shiraishi *et al.* reported that the original  $\text{O}_{\text{VS}}$  in  $\text{TiO}_2$  directly determined the efficiency of photocatalytic nitrogen fixation from water and  $\text{N}_2$ .<sup>4,5</sup> Zhang and co-workers found that the energy barrier of  $\text{N}_2$  reduction to ammonia could be remarkably decreased by elongating the  $\text{N}\equiv\text{N}$  triple bond *via* an end-on configuration between the adsorbed  $\text{N}_2$  and  $\text{O}_{\text{VS}}$  on the  $\text{BiOBr}$  surface.<sup>2,15</sup> It was also reported that the  $\text{O}_{\text{VS}}$  in  $\text{Bi}_2\text{MoO}_6$  played an important role in the  $\text{N}\equiv\text{N}$  triple bond splitting.<sup>16,17</sup> The  $\text{O}_{\text{VS}}$  in LDH nanosheets enhanced the adsorption and activation of  $\text{N}_2$  and  $\text{H}_2\text{O}$ , which made them show excellent photocatalytic activity for  $\text{N}_2$  reduction.<sup>18</sup>

Molybdenum trioxide ( $\text{MoO}_3$ ) has been extensively explored as a photochromic and electrochromic material due to

<sup>a</sup> School of Advanced Materials, Peking University, Shenzhen Graduate School, China. E-mail: meizw@pkusz.edu.cn, panfeng@pkusz.edu.cn

<sup>b</sup> Department of Materials Science and Engineering, Southern University of Science and Technology, China. E-mail: gum@sustc.edu.cn

† Electronic supplementary information (ESI) available: SEM, BET, XRD, TEM, colour change of samples, density of states (DOS) of the (001) plane, ion chromatography images and tables of oxygen formation energy, atomic populations (Mulliken) of the  $\text{Mo}_4\text{O}_{12}$  unit cell and  $\text{Mo}_4\text{O}_{11}$  unit cell, and summary of some metal oxides. See DOI: 10.1039/c8cy02357c

its unique energetic and electrical properties.<sup>19–21</sup> Oxygen vacancy-rich  $\text{MoO}_{3-x}$  has an unusual oxygen defect structure and novel properties in the nanometer regime.<sup>22,23</sup> It has been successfully used to photocatalyze isopropyl alcohol to propylene under visible light.<sup>24</sup> Besides, electrocatalytic nitrogen fixation of  $\text{MoO}_3$  has also shown good activity in a recent study.<sup>25</sup> However, there are few reports about photocatalytic  $\text{N}_2$  reduction by  $\text{MoO}_{3-x}$ . In this work,  $\text{MoO}_{3-x}$  nanobelts were synthesized by a simple one-pot hydrothermal method as previously described.<sup>24</sup> In comparison with the annealed sample in air, it was found that the  $\text{O}_{\text{VS}}$  on the surface of  $\text{MoO}_{3-x}$  can chemisorb and reduce the activation energy of  $\text{N}_2$  molecules, playing a critical role in determining the photocatalytic activity for  $\text{N}_2$  reduction.

## Experimental

### Materials and methods

In a typical synthesis, 0.36 g of molybdenum acetylacetonate was added into 40 ml of distilled water. Then the obtained solution was loaded into a stainless steel Teflon-lined autoclave and the sealed autoclave was kept at 180 °C for 20 h. After naturally cooling to room temperature, the blue product was washed with distilled water several times to remove any ions and possible remnants and subsequently dried at 50 °C for 12 h in a vacuum oven. For comparison, the as-synthesized products were annealed at 400 °C in a tube furnace in air atmosphere for  $x$  minutes ( $x = 0, 1, 5, \text{ and } 30$ ) to reduce surface oxygen vacancy concentration, and the final reactants are denoted as  $\text{MoO}_{3-x}$  min.

### Characterization of the photocatalysts

X-ray diffraction (XRD, Bruker, D8 Advance X-ray diffractometer) was used to characterize the crystal structure of the samples with the scanning range of  $2\theta$  from 10° to 50°. The morphology of the samples was observed on a field emission scanning electron microscope (FE-SEM, ZEISS SUPRA-@-55). The STEM and EELS analyses were performed on a Double-Cs aberration-corrected Themis G2 microscope at 300 kV with a Quantum GIF detector. UV-vis absorption spectroscopy was carried out on a UV-2450 (Shimadzu). X-ray photoelectron spectroscopy (XPS) was performed on a Thermo Scientific ESCALAB 250 Xi system. The Raman spectra were measured using a Horiba iHR 320 with a 532.1 nm laser as the excitation light, and the accumulation time was 25 s. The specific surface areas of the samples were determined through  $\text{N}_2$  adsorption–desorption isotherms at 77 K using an accelerated surface area and porosimetry system (ASAP, 2020 HD88). Electron spin resonance (ESR) spectroscopy was carried out using a Bruker A300, German under a magnetic field from 3400 to 3600 G. The temperature-programmed desorption of  $\text{N}_2$  ( $\text{N}_2$ -TPD) was tested with an Autosorb-iQ-C chemisorption analyser (Quantachrome, USA) with the temperature from 0 to 773 K.

### Photocatalytic $\text{N}_2$ fixation

The photocatalytic performance of the sample for  $\text{N}_2$  reduction was evaluated by the production rate of  $\text{NH}_4^+$  under full spectrum illumination without any sacrificial agents at room temperature and atmospheric pressure. The light source was a 300 W xenon lamp (CEL-HXF300, wavelength: 300–2500 nm, radiant output 50 W) and LEDs with wavelengths of 365 nm, 385 nm, 400 nm and 427 nm (UVEC-4II). A water circulation system was used to maintain the temperature at 25 °C. In each experiment, 50 mg of the photocatalyst was added and dispersed in 100 mL of distilled water, and then the mixture was kept under stirring and irradiated from the top-window with a  $\text{N}_2$  flow at a rate of 60 mL  $\text{min}^{-1}$ . 3 mL of the solution was taken out after every 2 h during the illumination. The catalyst in the sample was removed by centrifugation with a rotation rate of 16 000  $\text{r min}^{-1}$  for 5 min and then was filtered two times. Finally, the photocatalytic product was determined by ion chromatography (Metrohm IC). The photocatalyst was recycled after the photocatalytic experiment by centrifugation and then was filtered several times. And the recycling photocatalytic experiment was carried out with a 300 W xenon lamp.

### DFT calculations

All calculations were performed with the plane-wave projector-augmented wave method,<sup>26,27</sup> as implemented in the CASTEP package. The Perdew–Burke–Ernzerhof (PBE) form of generalized gradient approximation (GGA) was chosen as the exchange–correlation potential.<sup>28,29</sup> The PBE +  $U$  approach with spin polarization was employed to take account of the strong on-site Coulomb interaction ( $U$ ), present in the localized 4d electrons of Mo with  $U$  values being set to 2 eV. The cutoff energy for the plane wave was 340 eV. The integration in the Brillouin zone was carried out on a set of  $k$ -points determined by the Monkhorst and Pack scheme,  $4 \times 1 \times 4$ . Convergence was assumed when the total energy difference was less than  $10^{-6}$  eV between cycles of self-consistent iterations. Based on the results of the STEM analysis, a unit cell with one O vacancy at the 2c site ( $\text{Mo}_4\text{O}_{11}$ ) was used to perform the geometry-optimization calculations. The atomic populations (Mulliken) were analyzed after optimization. Furthermore, the binding energy of O-deficient Mo atoms in this structure model was further calculated by removing another coordinating O atom. In comparison, the perfect unit cell of  $\text{MoO}_3$  ( $\text{Mo}_4\text{O}_{12}$ ) was also calculated with the same calculation configurations.

The calculation of the N–N bond was performed using the first-principles density functional theory (DFT) +  $U$  calculations with the exchange–correlation energy functional, which were described by a generalized gradient approximation with the Perdew–Burke–Ernzerhof (PBE) exchange–correlation function.<sup>28</sup> We also took van der Waals interactions into correction by the DFT-D2 method of Grimme.<sup>30</sup> To simulate  $\text{N}_2$  activation on the  $\text{MoO}_3$  (001) and (100) surfaces, ( $2 \times 1 \times 3$ ) and ( $3 \times 1 \times 2$ ) supercells were used, respectively, enabled by

a VASP code in which the projector-augmented wave (PAW) method presented the electron-ion interaction with a kinetic energy cutoff of 520 eV.<sup>27,31</sup> The  $k$ -points were  $8 \times 4 \times 1$ ,  $4 \times 4 \times 1$  and  $4 \times 8 \times 1$  for each supercell. During optimizations, the energy and force converged to  $10^{-4}$  eV per atom and  $0.02$  eV  $\text{\AA}^{-1}$ , respectively.

## Results and discussion

The XRD patterns of the as-synthesized and annealed samples with different times are shown in Fig. 1a. All the peaks can be indexed to orthorhombic  $\text{MoO}_3$  (o- $\text{MoO}_3$ ) whose  $2\theta$  values are located at  $12.8^\circ$ ,  $23.4^\circ$ ,  $25.7^\circ$ ,  $25.8^\circ$ ,  $27.3^\circ$  and  $39.0^\circ$ . The result is consistent with previous reports.<sup>32,33</sup> After annealing, the XRD patterns of the annealed samples don't show an obvious shift as presented in Fig. 1a. The SEM images of the as-synthesized and annealed products are shown in Fig. S1.† It can be observed that the products are all composed of nanobelts, and the morphologies remain stable even after annealing. In addition, as shown in the HRTEM image, a  $\text{MoO}_{3-x}$  nanobelt is single crystalline and the inserted diffraction pattern in Fig. 1c proves the single-crystalline nature of the  $\text{MoO}_{3-x}$  nanobelt. Detailed analysis for fringing the formation of oxygen vacancies was performed using atomic scale HAADF Z-contrast images in Fig. 1d. Ordered oxygen vacancies residing at certain crystal plane surfaces often show up as dark-lines in a Z-contrast image due to the reduced average atomic density.<sup>34</sup> As shown in Fig. 1d, the white arrows point to the ordered oxygen vacancies residing at the (001) & (100) surfaces of  $\text{MoO}_{3-x}$ , where we observed such dark-lines along these surface planes. In addition, the red lines mark

the dislocation formed in  $\text{MoO}_{3-x}$ . The dislocations formed in the  $\text{MoO}_{3-x}$  may partially release the internal strain induced by the formation of such oxygen vacancies.

In order to prove the changes of  $\text{O}_{\text{VS}}$ , the fine structures of the electron energy loss spectroscopy (EELS) edges were further measured. The EELS edges reflect the unoccupied local density of states and therefore, provide useful local oxidation states and coordination chemistry of materials.<sup>35</sup> The Mo and O EELS results of the as-obtained  $\text{MoO}_{3-x}$  and  $\text{MoO}_{3-x}$  after 30 min annealing were acquired and plotted in Fig. 2 for comparison. The lattice distortion and reduced symmetry at the oxygen-deficient  $\text{MoO}_{3-x}$  certainly caused changes in the oxygen K edges. As reported by previous literature studies, the enhancement of a peak labelled by the red arrow is a signature of the formation of oxygen vacancies.<sup>36</sup> Another interesting feature to notice is the decreased intensity of the third peak as pointed by the purple arrow in the  $\text{MoO}_{3-x}$  sample compared with the  $\text{MoO}_{3-x}$  after 30 min annealing. Based on the multiple-scattering theory, the decreased intensity is caused by a decrease in the number of backscattering  $\text{O}^{2-}$  ions at the first or second-nearest oxygen neighbours, further proving the presence of oxygen vacancies in the  $\text{MoO}_{3-x}$  sample.<sup>37</sup>

The UV-vis absorption spectra of the samples in Fig. 3a were transformed from their reference spectra based on the Kubelka-Munk formula. There is a tail absorption for each sample, which results from the  $\text{O}_{\text{VS}}$ ,<sup>17</sup> and decreases gradually as the annealing time increases. The colour of the sample gradually turns white after the heat treatment as shown in Fig. S2.† These results indicate that the annealing treatment can remove the  $\text{O}_{\text{VS}}$  in the samples.

The Raman spectroscopy characterization results are shown in Fig. 3b. The Raman peaks of the as-synthesized  $\text{MoO}_{3-x}$  nanobelts are in agreement with those of previous research.<sup>38</sup> The peak at  $819\text{ cm}^{-1}$  shows a strong and well-defined line, assigned to the doubly coordinated bridging oxygen (Mo-O-Mo units). A couple of weak peaks at 461 and



Fig. 1 (a) XRD patterns of the as-synthesized and annealed  $\text{MoO}_{3-x}$  nanobelts for various times; (b) HAADF STEM image of the overall morphology of the  $\text{MoO}_{3-x}$  nanobelts; (c) HRTEM image of  $\text{MoO}_{3-x}$  with the insert showing the electron diffraction pattern; (d) atomic scale HAADF image showing the ordered oxygen vacancies at the (001) & (100) planes.

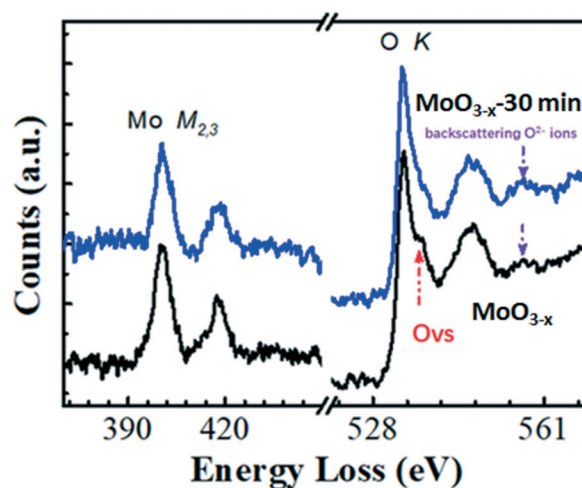


Fig. 2 EELS analysis of the as-synthesized  $\text{MoO}_{3-x}$  and  $\text{MoO}_{3-x}$  after 30 min annealing in air atmosphere.



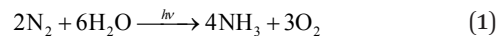
Fig. 3 (a) UV-vis absorption spectra, (b) Raman spectra, (c) Mo 3d-related XPS spectra, and (d) O 1s-related XPS spectra of the as-synthesized and annealed  $\text{MoO}_{3-x}$  for different times.

$676\text{ cm}^{-1}$  are attributed to the triply coordinated oxygen ( $\text{Mo}_3\text{-O}$ ). The peak at  $996\text{ cm}^{-1}$  consists of the terminal oxygen ( $\text{Mo}=\text{O}$ ) stretching mode. Both the XRD patterns and Raman spectra indicate that the prepared  $\text{MoO}_{3-x}$  nanobelts belong to an orthorhombic phase. However, there is no obvious shift in the Raman spectra of the annealed samples for different times, and it may result from the fact that the reduced  $\text{O}_{\text{VS}}$  by annealing are not capable enough to change the Raman characteristics. Besides, we have tried to choose lower annealing temperatures ( $150\text{ }^\circ\text{C}$ ,  $200\text{ }^\circ\text{C}$ , and  $300\text{ }^\circ\text{C}$ ) in our study before ensuring  $400\text{ }^\circ\text{C}$  as the final annealing temperature. And it is found that there was no obvious change in the sample colour although the annealing time was 1 h at  $300\text{ }^\circ\text{C}$  (Fig. S3<sup>†</sup>), indicating that the  $\text{O}_{\text{VS}}$  do not decrease very much. On the other hand, the structure of the samples is stable after  $400\text{ }^\circ\text{C}$  annealing, because the XRD and Raman results are similar (Fig. 1a and 3b) for the as-synthesized and annealed samples. However, the absorption coefficient of the UV-vis tail absorption (Fig. 3a) decreases as the annealing time increases. This proves that  $\text{O}_{\text{VS}}$  were drastically removed and the crystal structure remained stable after annealing at  $400\text{ }^\circ\text{C}$ .

The X-ray photoelectron spectra (XPS) are presented in Fig. 3c and d. For the as-synthesized  $\text{MoO}_{3-x}$  nanobelts, the peaks at  $232.3\text{ eV}$  and  $235.6\text{ eV}$  could be ascribed to the  $3d_{5/2}$  and  $3d_{3/2}$  orbitals of Mo 3d, respectively.<sup>39,40</sup> In Fig. 3d, the peaks at  $531.4\text{ eV}$  originate from the lattice oxygen anions.<sup>41</sup> After annealing, the peaks of Mo 3d gradually left-shift as the annealing time is increased. Similar phenomena are observed for the O 1s orbital as shown in Fig. 3d. In order to understand the deep reasons, the Mulliken electronegativity of the Mo and O elements of  $\text{MoO}_3$  with 25% or without  $\text{O}_{\text{VS}}$  was calculated using CASTEP (see details in the Experimental section).  $\text{Mo}_4\text{O}_{12}$  and  $\text{Mo}_4\text{O}_{11}$  were chosen as the unit cells in this theoretical calculation, corresponding to the non-defect and defect  $\text{MoO}_3$ , respectively. The calculation results are shown in Table S1.<sup>†</sup> The average charges for Mo and O in the

non-defect  $\text{MoO}_3$  are 1.44 and  $-0.451$ , respectively. The corresponding values are 1.37 and  $-0.499$  for the defect  $\text{MoO}_3$ , respectively. Obviously, Mo and O in the defect  $\text{MoO}_3$  show more negative charges than those in the non-defect  $\text{MoO}_3$ , which result in the increasing binding energy for Mo 3d and O 1s in the decreasing oxygen defect samples as shown in Fig. 3c and d.<sup>42</sup> Besides, the results of binding energy for  $\text{Mo}_4\text{O}_{12}$  and  $\text{Mo}_4\text{O}_{11}$  have also been calculated. In comparison with  $\text{Mo}_4\text{O}_{12}$ , the binding energy of  $\text{Mo}_4\text{O}_{11}$  ( $7.64\text{ eV}$ ) becomes smaller than that of  $\text{Mo}_4\text{O}_{12}$  ( $8.52\text{ eV}$ ), which also confirms the weaker chemical bond of Mo–O in the sample with higher  $\text{O}_{\text{VS}}$  concentration.

The photocatalytic performance was characterized under the irradiation of a 300 W xenon lamp with full spectra, and the quantity of the photo-fixed  $\text{NH}_4^+$  was determined using an ion chromatograph. Compared with the traditional method (Nessler's reagent), the ion chromatograph could detect  $\text{NH}_4^+$  more accurately and the measurement results would not be influenced by any organic reagents during the reaction.<sup>43</sup> Pure water was used as the solvent and proton source in this work. Generally, the chemical reaction from  $\text{N}_2$  to  $\text{NH}_3$  in neutral solution can be described as the following equation:<sup>44</sup>



The photocatalytic nitrogen fixation activity is shown in Fig. 4 (the representative original data from ion chromatography are shown in Fig. S4<sup>†</sup>). The as-synthesized  $\text{MoO}_{3-x}$  exhibits the highest  $\text{NH}_3$  production rate reaching nearly  $11.1\text{ }\mu\text{mol L}^{-1}\text{ g}^{-1}\text{ h}^{-1}$ , while the production rate is just a quarter remaining for the  $\text{MoO}_{3-x-1\text{ min}}$  sample. In addition, there is no detectable  $\text{N}_2$  reduction product for the  $\text{MoO}_{3-x-5\text{ min}}$  and  $\text{MoO}_{3-x-30\text{ min}}$  samples. As we know, the BET surface area is

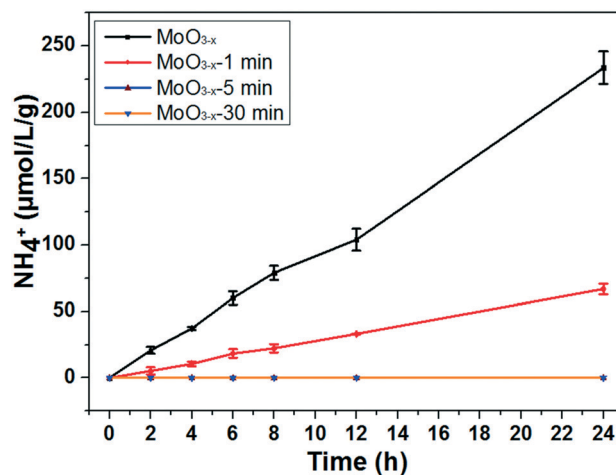


Fig. 4 Photocatalytic experiments for nitrogen fixation of the as-synthesized and annealed  $\text{MoO}_{3-x}$  nanobelts (light source: 300 W xenon lamp; photocatalyst: 0.05 g; solution: 100 ml of pure water. The error bar results came from photocatalytic experiments of the same samples performed three times.)

also a significant parameter for the photocatalytic activity. However, the surface areas are all around  $20 \text{ m}^2 \text{ g}^{-1}$  (Fig. S5<sup>†</sup>). Accordingly, the surface area can't obviously affect the photocatalytic  $\text{N}_2$  reduction activity. Furthermore, the light absorption of  $\text{MoO}_{3-x}$  5 min doesn't show great difference in comparison with that of the as-synthesized sample, but its photocatalytic product is undetectable. To find out the reason, electron spin resonance (ESR) spectroscopy and temperature-programmed desorption of  $\text{N}_2$  ( $\text{N}_2$ -TPD) were used to investigate the  $\text{O}_{\text{VS}}$  and  $\text{N}_2$  adsorption on the surface  $\text{O}_{\text{VS}}$ . In Fig. 5a, a signal exists at  $g = 2.001$  caused by  $\text{O}_{\text{VS}}$  in the as-synthesized and annealed samples.<sup>45</sup> However, there are no obvious changes even if the samples are annealed for 30 minutes at  $400^\circ\text{C}$ . This must result from the fact that the  $\text{O}_{\text{VS}}$  have not been totally removed in the whole sample. In Fig. 5b, a single desorption peak of  $\text{N}_2$  begins at  $180^\circ\text{C}$  and centers at  $320^\circ\text{C}$  for the as-synthesized sample, which is ascribed to the chemisorbed  $\text{N}_2$ .<sup>2</sup> However, the peak becomes weaker obviously for sample  $\text{MoO}_{3-x}$  5 min and disappears for sample  $\text{MoO}_{3-x}$  30 min. These results indicate that the surface  $\text{O}_{\text{VS}}$  were gradually removed but there were still  $\text{O}_{\text{VS}}$  in the inner part of the annealed samples. Compared with the photocatalytic activities in Fig. 4, samples  $\text{MoO}_{3-x}$  5 min and  $\text{MoO}_{3-x}$  30 min don't show detectable products, which must be caused by the disappearance of enough surface  $\text{O}_{\text{VS}}$ . In other words, the surface  $\text{O}_{\text{VS}}$  are the key factor for the efficient photocatalytic  $\text{N}_2$  reduction.

The reported photocatalytic activities of typical metal oxides were compared, which were characterized in pure water under UV-vis light irradiation (Table S2<sup>†</sup>). Hirakawa and co-workers created  $\text{Ti}^{3+}$  as active sites in  $\text{TiO}_2$  which exhibited an  $\text{NH}_3$  production rate of  $35.0 \mu\text{mol g}^{-1} \text{ h}^{-1}$ .<sup>45</sup> Zhang *et al.* reported that the  $\text{NH}_3$  production of Mo-doped  $\text{W}_{18}\text{O}_{49}$  reached  $61.9 \mu\text{mol g}^{-1} \text{ h}^{-1}$ .<sup>46</sup> Most other reported metallic oxides exhibited production rates around  $0.41$ – $28.4 \mu\text{mol g}^{-1} \text{ h}^{-1}$ .<sup>47–51</sup> The as-synthesized  $\text{MoO}_{3-x}$  nanobelts show this production in the middle range.

It could be seen that there was strong IR absorption even at  $850 \text{ nm}$  from the UV-vis absorption (Fig. 3a). The photocatalytic performance was further characterized under LED irradiation with different wavelengths to find out the connection between the light wavelength and  $\text{NH}_3$  synthesis. LEDs with wavelengths of  $365 \text{ nm}$ ,  $384 \text{ nm}$ ,  $400 \text{ nm}$ , and  $427 \text{ nm}$  were used as the light source. The results have been normal-

ized because of the different powers of LEDs. As shown in Fig. 6a, the LED with a wavelength of  $365 \text{ nm}$  exhibits the highest  $\text{NH}_3$  production rate reaching nearly  $3.3 \mu\text{mol L}^{-1} \text{ g}^{-1} \text{ h}^{-1} \text{ W}^{-1}$ , while  $\text{NH}_3$  production is not detected in the reaction irradiated by  $400$  and  $427 \text{ nm}$  LEDs. This means that the sample could only fix  $\text{N}_2$  under ultraviolet light irradiation ( $\lambda < 400 \text{ nm}$ ) although there was still light absorption in the longer wavelength range ( $\lambda \geq 400 \text{ nm}$ ). In addition, the quantum efficiency (QE) was also calculated by the following equation:<sup>52</sup>

$$\text{QE} = \frac{\text{rate of reaction induced by photon absorp}}{\text{flux of absorbed photons}} = \frac{3 \times n_{\text{NH}_4^+} \times N_0}{\frac{PS\lambda}{hc} \times t \times \alpha} \quad (2)$$

where  $P$  is the optical power density of the LED,  $S$  is the area of the illumination,  $t$  is the reaction time and  $\alpha$  is the light absorption. Here it has been supposed that all of the light energy was absorbed during the photocatalytic reaction. The optical power was measured to be  $325 \text{ mW}$  for the  $365 \text{ nm}$  LED, and the calculated value of QE at  $365 \text{ nm}$  was about  $0.013\%$ .

To ensure the source of the N element, argon was used to replace the  $\text{N}_2$  as the gas source after illumination for  $6 \text{ h}$  under a  $\text{N}_2$  flow. Obviously, the  $\text{N}_2$  fixation reaction hardly occurs under the Ar flow because the amount of  $\text{NH}_4^+$  doesn't increase (Fig. 6b). This result indicates that the N atoms in  $\text{NH}_3$  come from  $\text{N}_2$ . Besides, recycling photocatalytic experiments were also carried out to characterize the photochemical stability of  $\text{MoO}_{3-x}$ . It has been found that the  $\text{NH}_3$  production is just  $70\%$  remaining during the first cycle, and  $65\%$  remaining for the second cycle (Fig. S6a<sup>†</sup>). The possible reason is that some  $\text{O}_{\text{VS}}$  are inactive for the further photocatalytic  $\text{N}_2$  fixation after each cycle, because there are no obvious change for the XRD and TEM results of the sample before and after reaction (Fig. S7 and S8<sup>†</sup>). Moreover, we have also studied the effect of catalyst dosage on photocatalytic activities. As shown in Fig. S6b<sup>†</sup>, the rate of  $\text{NH}_3$  production would be enhanced obviously if the quantity of the catalyst is increased (nearly  $1 \mu\text{mol L}^{-1}$  for  $50 \text{ mg}$  of catalysts, while  $4 \mu\text{mol L}^{-1}$  for  $1 \text{ g}$  of catalysts). However, the rates of  $\text{NH}_3$  production decrease if the value is converted to one gram. It is

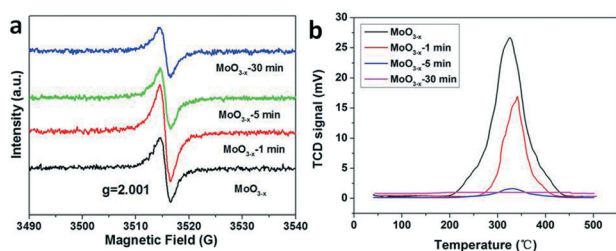


Fig. 5 (a) ESR spectra and (b)  $\text{N}_2$ -TPD profiles of the as-synthesized and annealed samples for different times.

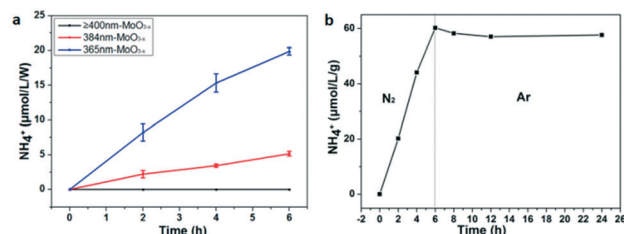


Fig. 6 (a) Photocatalytic activities for nitrogen fixation of the as-synthesized  $\text{MoO}_{3-x}$  nanobelts under LED light irradiation with various wavelengths; (b) control experiment in  $\text{N}_2$  and Ar gas in succession for photocatalytic nitrogen fixation (light source:  $300 \text{ W}$  xenon lamp).

reasonable that the larger dosage of the catalyst cannot be exposed enough to light for photocatalytic  $N_2$  fixation. Then a larger dosage of the catalyst exhibits a lower photocatalytic activity when converting to  $\mu\text{mol L}^{-1} \text{g}^{-1}$ .

Based on the result of the electron diffraction pattern in Fig. 1c, the (100) and (001) planes exist in the  $\text{MoO}_{3-x}$  nanobelts. Theoretical calculation was carried out to further study the formation energy of  $O_{\text{VS}}$  in these two planes. As shown in Fig. 7, there are three and four kinds of O-sites on the (001) and (100) planes, respectively. The calculation results are shown in Table S3.† For the (001) plane, the  $O_{\text{VS}}$  formation energy on the O1 site is equal to that on the O2 site (1.05 eV), which is more stable than that on the O3 site (1.29 eV). This means that it is easier to form  $O_{\text{VS}}$  on the O1 (O2) site. For the (100) plane, the formation energy on the O1 and O2 sites is equal to  $-1.97$  eV, and the value is 2.24 eV on the O3 and O4 sites. These results indicate that the  $O_{\text{VS}}$  are easier to form on the O1 and O2 sites of the (001) plane, and the  $O_{\text{VS}}$  can spontaneously form on the O1 and O2 sites of the (100) plane.

The density of states of the (001) plane with or without  $O_{\text{VS}}$  was calculated to explain the electron transfer processes during  $O_{\text{VS}}$ -mediated photocatalytic nitrogen fixation (Fig. S9†). When there are  $O_{\text{VS}}$  on the (001) plane, some defect levels appear between the valence and conduction bands. This also explains why there is tail absorption for defect  $\text{MoO}_{3-x}$  (Fig. 3a and 8a). Due to the lower energy of the defect levels, the photoexcited electrons on the conduction band will move to the defect levels, and the  $O_{\text{VS}}$  thus act as the trap sites of electrons. Subsequently, the photoexcited electrons with enough energy will reduce the chemically adsorbed  $N_2$  by  $O_{\text{VS}}$  into  $\text{NH}_3$ .

Additionally, the theoretical calculation was carried out to further study the function of surface  $O_{\text{VS}}$  for  $N_2$  photofixation. When there are no  $O_{\text{VS}}$  on the surface of  $\text{MoO}_3$ , the  $N_2$  molecule floats above the surface of the catalyst, and the  $N\equiv N$  triple bond length (1.113 Å) doesn't change (Fig. 8b). There are two models including end-on and side-on ways for nitrogen adsorption on the  $O_{\text{VS}}$  on the (001) surface and (100) surface where the  $O_{\text{VS}}$  are located as confirmed by atomic scale HAADF (Fig. 1d) and the above discussion. Based on the theoretical calculation results, there is little possibility for end-on ways on the (001) surface and side-on ways on the (100)

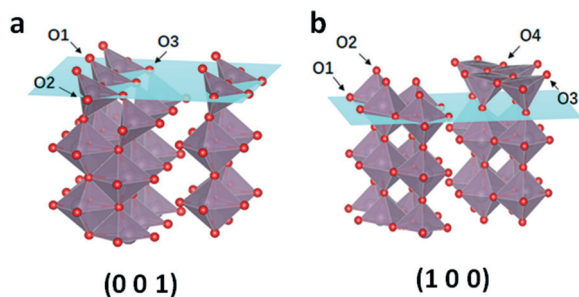


Fig. 7 (a) Three kinds of O sites on the (001) plane and (b) four kinds of O sites on the (100) plane.



Fig. 8 (a) Electron transfer processes during  $O_{\text{VS}}$ -mediated nitrogen fixation. (b)  $N_2$  adsorbed on the pristine surface; (c) terminal side-on adsorption on (001) and (d) end-on bridging adsorption on (100) for  $N_2$  (yellow means increasing charge and blue means decreasing charge).

surface for nitrogen adsorption, respectively, due to the reason that their adsorptions are too unstable to produce models for further calculation.

The bond length N1–N2 is 1.152 Å and 1.157 Å as observed on the (001) surface in Fig. 8c and on the (100) surface in Fig. 8d, respectively.

Obviously, the bond length of the N–N bond is elongated for the adsorbed  $N_2$  molecule. In other words, the  $N_2$  molecule chemisorbs on the  $O_{\text{VS}}$  and its activation energy can be decreased, which is beneficial to photocatalytic  $N_2$  reduction to  $\text{NH}_3$ . Fig. 8c and d show the charge distribution of nitrogen by side-on adsorption on the (001) plane and end-on adsorption on the (100) plane, respectively. It is well-known that  $N_2$  molecule reduction needed electrons to change into  $\text{NH}_3$ . The Bader charge analysis in Fig. 8 demonstrates that there will be 0.34|e| electron on the (001) plane and 0.09|e| on the (100) plane transferring from the unsaturated Mo atom ( $O_{\text{VS}}$ ) to the  $N_2$  molecule, respectively. When the semiconductor is irradiated by light, the photoexcited electrons can be successfully injected from the  $O_{\text{VS}}$  into the  $N_2$  molecule for its reduction reaction.

## Conclusions

In summary, we have successfully synthesized o- $\text{MoO}_{3-x}$  by a simple one-pot hydrothermal method and tested its photocatalytic nitrogen fixation activity in pure water for the first time. We found that the  $O_{\text{VS}}$  were located on the (001) plane and (100) plane by STEM measurement. The surface  $O_{\text{VS}}$  play a critical role in the photocatalytic  $N_2$  reduction by

chemisorption and the activation energy decrease of nitrogen molecules. The N<sub>2</sub> molecule prefers to adsorb on the O<sub>VS</sub> by the side-on model on the (001) plane and the end-on model on the (100) plane, respectively. Our findings can provide useful information for further development of other efficient photocatalysts for N<sub>2</sub> reduction.

## Conflicts of interest

There are no conflicts of interest to declare.

## Acknowledgements

This research was financially supported by Guangdong key lab Project (2017B030301013), Shenzhen Science (JCYJ20151015162256516), Technology Research Grant (JCYJ20160226105838578), National Key R&D Program of China (2016YFB0700600), and the Shenzhen Peacock Plan (KQTD2014062714543296).

## Notes and references

- 1 D. E. Canfield, A. N. Glazer and P. G. Falkowski, *Science*, 2010, **330**, 192–196.
- 2 H. Li, J. Shang, Z. Ai and L. Zhang, *J. Am. Chem. Soc.*, 2015, **137**, 6393–6399.
- 3 G. N. Schrauzer and T. D. Guth, *J. Am. Chem. Soc.*, 1977, **99**, 7189–7193.
- 4 H. Hirakawa, M. Hashimoto, Y. Shiraiishi and T. Hirai, *ACS Catal.*, 2017, **7**, 3713–3720.
- 5 Z. Dai, F. Qin, H. Zhao, J. Ding, Y. Liu and R. Chen, *ACS Catal.*, 2016, **6**, 3180–3192.
- 6 J. Ding, Z. Dai, F. Qin, H. Zhao, S. Zhao and R. Chen, *Appl. Catal., B*, 2017, **205**, 281–291.
- 7 Q. Wang, W. Wang, L. Zhong, D. Liu, X. Cao and F. Cui, *Appl. Catal., B*, 2018, **220**, 290–302.
- 8 Q. Wang, Z. Liu, D. Liu, G. Liu, M. Yang, F. Cui and W. Wang, *Appl. Catal., B*, 2018, **236**, 222–232.
- 9 F. Tian, H. Zhao, G. Li, Z. Dai, H. Zhao, Y. Liu and R. Chen, *ChemSusChem*, 2016, **9**, 1579–1585.
- 10 D. Tio, *Nanoscale*, 2013, **5**, 3601–3614.
- 11 X. Chen, L. Liu, P. Y. Yu and S. S. Mao, *Science*, 2011, **331**, 746–751.
- 12 J. Ding, Z. Dai and F. Tian, *J. Mater. Chem. A*, 2017, **5**, 23453–23459.
- 13 K. C. MacLeod, D. J. Vinyard and P. L. Holland, *J. Am. Chem. Soc.*, 2014, **136**, 10226–10229.
- 14 S. Wang, X. Hai, X. Ding, K. Chang, Y. Xiang, X. Meng, Z. Yang, H. Chen and J. Ye, *Adv. Mater.*, 2017, **29**, 1–7.
- 15 J. Li, H. Li, G. Zhan and L. Zhang, *Acc. Chem. Res.*, 2017, **50**, 112–121.
- 16 C. Shi, X. Dong, Y. Hao, X. Wang, H. Ma and X. Zhang, *RSC Adv.*, 2017, **7**, 50040–50043.
- 17 Y. Li, Y. Zhao, H. Cheng, Y. Hu, G. Shi, L. Dai and L. Qu, *J. Am. Chem. Soc.*, 2012, **134**, 15–18.
- 18 Y. Zhao, Y. Zhao, G. I. N. Waterhouse, L. Zheng, X. Cao, F. Teng, L. Z. Wu, C. H. Tung, D. O'Hare and T. Zhang, *Adv. Mater.*, 2017, **29**, 1–10.
- 19 H. Natori, K. Kobayashi and M. Takahashi, *J. Oleo Sci.*, 2009, **58**, 203–211.
- 20 Y. Yang, Y. Cao, B. Loo and J. Yao, *J. Phys. Chem. B*, 1998, **102**, 9392–9396.
- 21 M. Greenblatt, *Chem. Rev.*, 1988, **88**, 31–53.
- 22 S. G. Processes, N. Pinna and M. Niederberger, *Angew. Chem., Int. Ed.*, 2008, **47**, 5292–5304.
- 23 M. A. Ibrahim, F.-Y. Wu, A. Mengistie, C. Chang, D. A. Mengistie, L. Li, C. W. Chu and V. A. Online, *Nanoscale*, 2014, **6**, 5484–5490.
- 24 H. Bai, W. Yi, J. Li, G. Xi, Y. Li, H. Yang and J. Liu, *J. Mater. Chem. A*, 2016, **4**, 1566–1571.
- 25 J. Han, X. Ji, X. Ren, G. Cui, L. Li, F. Xie, H. Wang, B. Li and X. Sun, *J. Mater. Chem. A*, 2018, **6**, 12974–12977.
- 26 P. E. Blöchl, *Phys. Rev. B: Condens. Matter Mater. Phys.*, 1994, **50**, 17953–17979.
- 27 D. Joubert, *Phys. Rev. B: Condens. Matter Mater. Phys.*, 1999, **59**, 1758–1775.
- 28 J. P. Perdew, K. Burke and M. Ernzerhof, *Phys. Rev. Lett.*, 1996, **77**, 3865–3868.
- 29 V. I. Anisimov, M. A. Korotin, J. Zaanen and O. K. Andersen, *Phys. Rev. Lett.*, 1992, **68**, 345–348.
- 30 S. Grimme, T. O. Chemie and O. I. D. U. Münster, *J. Comput. Chem.*, 2006, **16**, 1787–1799.
- 31 G. Kresse and J. Furthmüller, *Phys. Rev. B: Condens. Matter Mater. Phys.*, 1996, **54**, 11169–11186.
- 32 N. Pinna and M. Niederberger, *Angew. Chem., Int. Ed.*, 2008, **47**, 5292–5304.
- 33 S. Hu and X. Wang, *J. Am. Chem. Soc.*, 2008, **130**, 8126–8127.
- 34 R. F. Klie and N. D. Browning, *Microsc. Microanal.*, 2018, **8**, 475–486.
- 35 D. A. Muller, *Nat. Mater.*, 2009, **8**, 263–270.
- 36 D. Wang, D. S. Su and R. Schlögl, *Z. Anorg. Allg. Chem.*, 2004, **630**, 1007–1014.
- 37 N. D. Browning, H. O. Moltaji and J. P. Buban, *Phys. Rev. B: Condens. Matter Mater. Phys.*, 1998, **58**, 8289–8300.
- 38 L. Seguin, M. Figlarz, R. Cavagnat and J. C. Lassegues, *Spectrochim. Acta, Part A*, 1995, **51**, 1323–1344.
- 39 M. A. Bica De Moraes, B. C. Trasferetti, F. P. Rouxinol, R. Landers, S. F. Durrant, J. Scarmínio and A. Urbano, *Chem. Mater.*, 2004, **16**, 513–520.
- 40 Q. Huang, S. Hu, J. Zhuang and X. Wang, *Chem. – Eur. J.*, 2012, **18**, 15283–15287.
- 41 J. Wang, Y. Xia, H. Zhao, G. Wang, L. Xiang, J. Xu and S. Komarneni, *Appl. Catal., B*, 2017, **206**, 406–416.
- 42 Z. Mei, M. Zhang, J. Schneider, W. Wang, N. Zhang, Y. Su, B. Chen, S. Wang, A. L. Rogach and F. Pan, *Catal. Sci. Technol.*, 2017, **7**, 982–987.
- 43 X. Gao, Y. Wen, D. Qu, L. An, S. Luan, W. Jiang, X. Zong, X. Liu and Z. Sun, *ACS Sustainable Chem. Eng.*, 2018, **6**, 5342–5348.
- 44 K. Tennakone, S. Punchihewa, S. Wickramanayake, C. A. N. A. N. Fernando, O. A. Illeperuma, O. A. Illeperuma and S. Punchihewa, *J. Chem. Soc., Chem. Commun.*, 1987, 1078–1080.

- 45 H. Hirakawa, M. Hashimoto, Y. Shiraishi and T. Hirai, *J. Am. Chem. Soc.*, 2017, **139**, 10929–10936.
- 46 N. Zhang, A. Jalil, D. Wu, S. Chen, Y. Liu, C. Gao, W. Ye, N. Zhang, A. Jalil, D. Wu, S. Chen, Y. Liu, C. Gao and W. Ye, *J. Am. Chem. Soc.*, 2018, **140**, 9434–9443.
- 47 Q. Li, K. Donmen, S. Naito, T. Onishi and K. Tamaru, *Chem. Lett.*, 1983, **2**, 321–324.
- 48 M. M. Khader, N. N. Lichtin, G. H. Vurens, M. Salmeron and G. A. Somorjai, *Langmuir*, 1987, **3**, 303–304.
- 49 J. Soria, J. C. Conesa, V. Augugliaro, L. Palmisano, M. Schiavello and A. Sclafani, *J. Phys. Chem.*, 1991, **95**, 274–282.
- 50 S. Sun, X. Li, W. Wang, L. Zhang and X. Sun, *Appl. Catal., B*, 2017, **200**, 323–329.
- 51 K. T. Ranjit and B. Viswanathan, *Indian J. Chem., Sect. A: Inorg., Bio-inorg., Phys., Theor. Anal. Chem.*, 1996, **35**, 443–453.
- 52 M. Liu, R. Inde, M. Nishikawa, X. Qiu, D. Atarashi, E. Sakai and Y. Nosaka, *ACS Nano*, 2014, **8**, 7229–7238.